Chemical Science

EDGE ARTICLE

View Article Online
View Journal | View Issue

Check for updates

Cite this: *Chem. Sci.*, 2019, **10**, 1193

All publication charges for this article have been paid for by the Royal Society of Chemistry

Received 8th October 2018
Accepted 12th November 2018

DOI: 10.1039/c8sc04464c

rsc.li/chemical-science

Rationally designed pure-inorganic upconversion nanoprobes for ultra-highly selective hydrogen sulfide imaging and elimination *in vivo*†

Yuxin Liu, Qi Jia, Xuejiao Zhai, Fang Mao, Anqi Jiang and Jing Zhou *

Lung injury is a hydrogen sulfide (H_2S)-associated complication with high mortality in acute pancreatitis (AP) cases. Herein, we used Prussian Blue (PB) as a H_2S-responsive acceptor to develop a novel pure-inorganic upconversion nanoprobe for detecting and eliminating H_2S, which can be used for diagnosing AP and alleviating lung injury. Upconversion nanoprobes with 5 nm PB shells were optimized to achieve outstanding *in vitro* H_2S detection capacity (linear range: 0–150 μM, LOD: 50 nM), which met the *in vivo* serum H_2S range, and thus were feasible for imaging H_2S *in vivo*. More importantly, when combined with the traditional H_2S synthetase inhibitor DL-PAG, the nanoprobes also served as a therapeutic agent that synergistically alleviated lung injury. As PB is an FDA-approved drug, our work proposes a potential clinical modality for the early diagnosis of AP, which will decrease lung injury-induced mortality and increase the survival rates of AP cases.

Introduction

Hydrogen sulfide (H_2S) is a newly discovered gaseous signaling molecule, in addition to nitrogen oxide and carbon monoxide, and is an essential player in various physiological processes.[1] In acute pancreatitis (AP) cases, excessive serum H_2S levels can cause lung injury, which leads to high early mortality rates due to respiratory failure and hypoxemia.[2,3] Therefore, developing a probe that can simultaneously image and eliminate H_2S from serum would significantly benefit AP patients.

Luminescence probes can be applied to disease diagnostics due to their strong performance in time-resolution imaging and dynamic bioinformatics monitoring.[4–11] Among all phosphors, upconversion nanoparticles emit adjustable luminescence (300–800 nm) under near-infrared (NIR) excitation, and have the advantages of low background luminescence and high stability, which makes them ideal for *in vivo* luminescence imaging.[12–16] Therefore, upconversion nanoparticles are feasible for use as donors in construction of high-performance luminescence nanoprobes.[17–21] Using upconversion nanoparticles as donors and H_2S-responsive acceptors, some upconversion nanoprobes for H_2S detection and imaging have been developed based on Förster resonance energy transfer (FRET) and inner filter effects.[22–24] However, the typical H_2S-responsive acceptors were organic dyes with obvious shortcomings, including low stability and hydrophobicity. In contrast, inorganic acceptors have no such issues, but are limited by low H_2S selectivity and potential toxicity to biosystems, which resulted in less research into inorganic acceptors. Thus, an exploration of biocompatible inorganic H_2S-responsive acceptors with good selectivity and high stability should be conducted with the aim of developing nontoxic hydrophilic H_2S nanoprobes.

Due to the strong interaction between Fe(II/III) and cyanide, Prussian Blue (PB) is ultra-stable when combined with various biomolecules, which contributes to its outstanding biocompatibility.[25] Nevertheless, a synchronous reaction between Fe(III) and H_2S may cause the decomposition of PB in a H_2S solution, which would result in decreased PB absorbance that can be used to colorimetrically detect H_2S. When applying PB as a H_2S-responsive acceptor to construct upconversion nanoprobes, the weakened absorbance in the visible and NIR ranges can also lead to upconversion luminescence (UCL) recovery, which can be used for luminescence detection of H_2S. Conversely, PB can also eliminate free H_2S in fluid by forming stable sulfur and sulfide compounds, which means that these nanoprobes could be a potential drug for eliminating excessive serum H_2S. As PB is a US Food and Drug Administration (FDA)-approved drug for clinical use, PB-modified upconversion nanoprobes may be optimal inorganic nanoprobes that simultaneously image and eliminate H_2S.

Herein, a novel PB-functionalized upconversion nanoprobe was developed for dual-modal colorimetric/luminescence H_2S detection. The thickness of the PB shell was modulated to achieve the optimal detection capacity within the serum H_2S concentration range. To ensure safety, the cytotoxicity, biocompatibility, and biobehavior of the as-optimized

Department of Chemistry, Capital Normal University, Beijing 100048, China. E-mail: jingzhou@cnu.edu.cn; Tel: +86-010-68902491

† Electronic supplementary information (ESI) available. See DOI: 10.1039/c8sc04464c

nanoprobes were carefully studied. Ultimately, the feasibility of the nanoprobes for imaging H_2S and alleviating lung injury was confirmed in an AP mouse model.

Results and discussion

Rationally designed upconversion nanoprobes for H_2S detection

The PB-functionalized upconversion nanoprobes were rationally designed as a core–shell structure of 20% Er-doped $NaLuF_4$:Yb,Er,Tm@$NaLuF_4$ nanoparticles (UCNPs) coated with a homogeneous PB shell of optimal thickness. Using typical solvothermal methods, uniform core–shell UCNPs were synthesized with a larger size distribution (47.2 ± 4.3 nm) than that of $NaLuF_4$:Yb,Er,Tm cores (37.2 ± 3.8 nm; Fig. 1A and S1A and B†). After inner shell coating, the upconversion luminescence (UCL) of UCNPs was significantly improved in both visible and NIR regions due to inhibition of multi-phonon relaxation between the emitter and the absorbed ligands (Fig. S1C†). Furthermore, X-ray diffraction (XRD) patterns suggested that the UCNPs were in a highly crystallized hexagonal phase, corresponding to the standard reference card of β-$NaLuF_4$ (JCPDS: 027-0726; Fig. S2A†). High-resolution transmission electron microscopy (HR-TEM) images of UCNPs with a defined crystallographic plane supported this finding (Fig. 1B).

To obtain the as-designed nanoprobes, a PB shell was coated onto UCNPs (UC-PB) by the ligand-exchange and controllable complexation method.[26] After successful PB coating, the low contrast shell could be identified in both HR-TEM and scanning transmission electron microscopy (STEM) images (Fig. 1C and D). Energy dispersive X-ray analysis (EDXA) line scanning

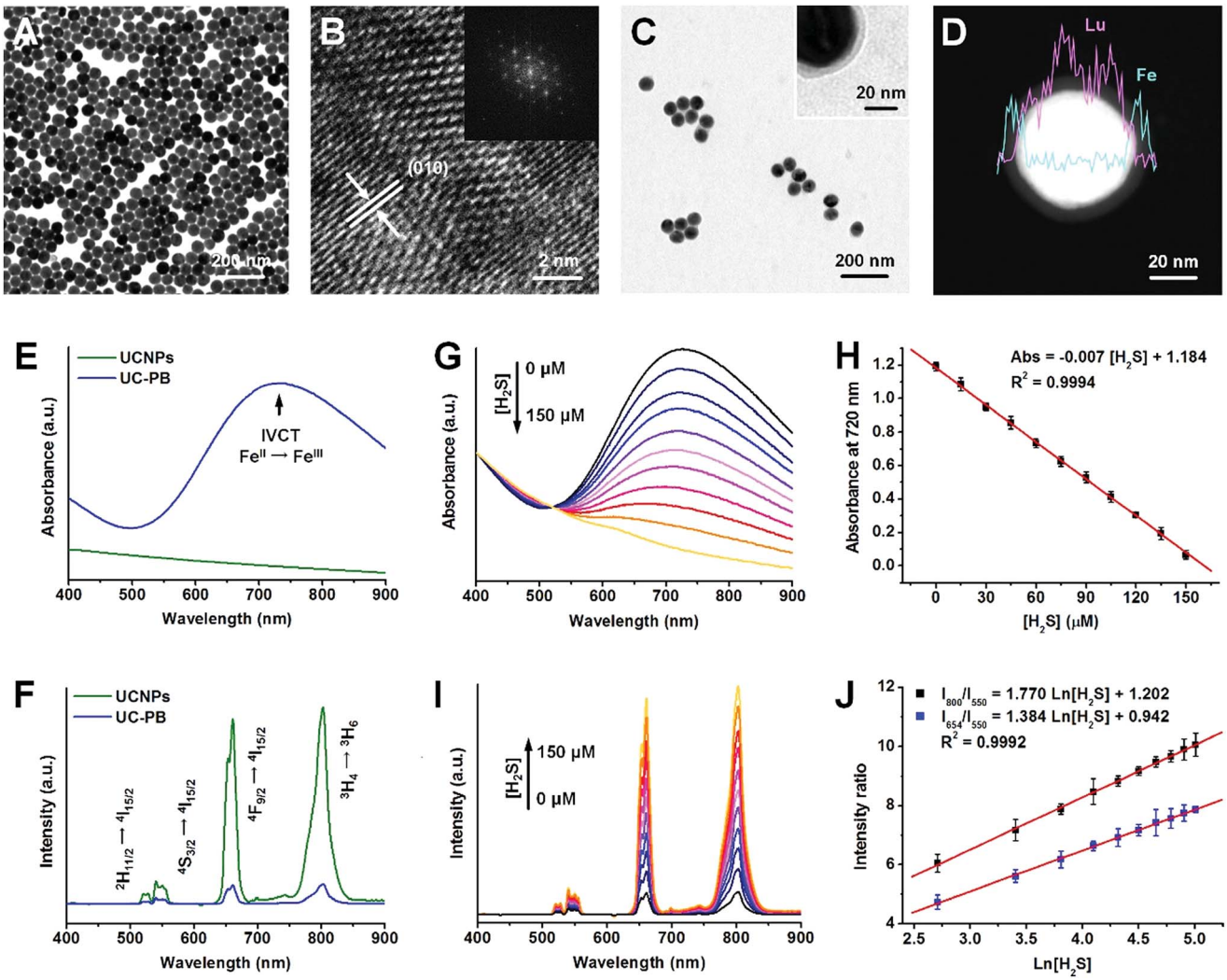

Fig. 1 Characterization and H_2S detection capacities of the UC-PB nanoprobe. TEM image (A) and high-resolution lattice image (B) of UCNPs. Inset: the corresponding fast Fourier transform diffractogram. (C) TEM image of the UC-PB nanoprobes. Inset: TEM image of a single UC-PB nanoprobe. (D) STEM image and EDXA line scan on a single UC-PB nanoprobe. UV-vis-NIR absorbance spectra (E) and UCL spectra (F) of UCNPs and UC-PB nanoprobes. UV-vis-NIR absorbance spectra (G) and UCL spectra (I) of UC-PB nanoprobes in response to various concentrations of H_2S. Linear relationship between absorbance at 720 nm (H) or between the UCL ratio (J) of UC-PB_5 nanoprobes and various concentrations of H_2S. Data are represented as mean ± SD.

results found that Fe was well-distributed on the periphery of UCNPs, which further confirmed the existence of the PB shell on UCNP surfaces (Fig. 1D). Furthermore, a new diffraction peak was observed at the 2-theta range of 20–40 degrees, which corresponded to the (2,2,0) and (3,3,1) crystallographic planes of face-centered cubic PB (JCPDS: 52-1907) and indicated PB formation in the as-prepared nanoprobes (Fig. S2B†). The Fe peak in the EDXA spectrum and fabrication of cyanide bonds in the Fourier transform infrared (FTIR) spectrum also illustrated successful PB coating (Fig. S2C and D†). The as-prepared nanoprobes had a strong absorbance peak in the red (600–700 nm) and NIR (700–900 nm) ranges (Fig. S3†), which was attributed to the intervalence charge transfer between Fe(III) and Fe(II) in PB and caused remarkable UCL quenching of UCNPs through both Förster resonance energy transfer (FRET) and inner filter effects (Fig. 1E and F and S4A†). Compared with typical upconversion nanoparticles with relatively low Er dopant concentration (2% Er dopant, UCNPs-L), these UCNPs (20% Er dopant) had stronger UCL in the red and NIR regions, and higher red/green and NIR/green ratios, which were well matched with the absorbance range of PB, and thus were more feasible for constructing PB-functionalized upconversion nanoprobes (Fig. S4B–D†).

As the H_2S concentration increased, the absorbance of PB decreased and the UCL of UCNPs recovered accordingly, owing to the decomposition of the PB shells in response to H_2S (Fig. 1G and I). To study and optimize the influence of PB thickness on H_2S detection performance, nanoprobes with 5 nm (UC-PB_5), 8 nm (UC-PB_8), and 11 nm (UC-PB_{11}) PB shells were prepared by modulating the reactant ratio (Fig. S5A and B†). As the concentration of serum H_2S is within the micromolar range (reported previously as 0–150 μM), the nanoprobes were optimized to be within this range. It was found that all three nanoprobes responded to H_2S, while the UCNP itself had no response (Fig. S5C–E†), which highlighted the essential role of PB in the H_2S-responsive nanoprobes. As changes in absorbance and UCL were highly correlated with the reacted PB ratio, nanoprobes with thinner PB shells showed higher H_2S sensitivity. However, low levels of PB limited the detection range due to limiting amounts of the H_2S responsive agent. When the PB shell was <5 nm, serum H_2S concentrations were beyond the detection range of the nanoprobes (Fig. S5C–E†). Meanwhile, compared with nanoprobes with thicker shells, UC-PB_5 had larger signal changes and was significantly more sensitive in the same H_2S concentration range. Therefore, to be within the serum H_2S concentration ranges while achieving the balance between a wide detection range and high sensitivity, UC-PB_5 nanoprobes were selected. These results also demonstrated that the range and sensitivity of H_2S detection could be easily modulated by changing the PB shell thickness, which demonstrated the great adaptability of the PB-functionalized nanoprobes.

Since UC-PB_5 nanoprobes were optimized for H_2S detection in clinical applications, a detailed evaluation of their performance was conducted. The concentration and absorbance at 720 nm of UC-PB_5 nanoprobe suspensions were quantified using ultraviolet-visible-near-infrared (UV-vis-NIR) spectra before being used for detection. We found that the absorbance at 720 nm of a UC-PB_5 nanoprobe suspension was negatively correlated with H_2S concentration at 0–150 μM (Abs. = 1.184 − 0.007 × [H_2S]/μM, $R^2 = 0.9994$, LOD: 10 nM, Fig. 1H). Moreover, using the 550 nm UCL intensity as a reference, the relative 654 nm (abbreviated I_{654}/I_{550}) and 800 nm (abbreviated I_{800}/I_{550}) intensities were positively linearly correlated with Ln[H_2S] within the same range ($I_{654}/I_{550} = 0.942 + 1.384 \times \mathrm{Ln}[H_2S]/\mu M$, $I_{800}/I_{550} = 1.202 + 1.770 \times \mathrm{Ln}[H_2S]/\mu M$, $R^2 = 0.9992$, LOD: 10 nM, Fig. 1J). Compared with all previously reported upconversion nanoprobes for H_2S detection, UC-PB_5 had a favorable detection capacity (Table S1†).[23,24,27,28] It is noteworthy that the reaction between UC-PB_5 and H_2S reached equilibrium within a very short period (approximately 350 s for the spectra and 20 s for the naked eye, Fig. S6 and Video S1†), which indicated that UC-PB_5 was feasible for dynamic H_2S detection. More importantly, UC-PB_5 nanoprobes were well-dispersed in various biological fluids and showed high stability after long-term storage (Fig. S7†). Therefore, UC-PB_5 can serve as a dual-modal colorimetric/luminescence probe with favorable biostability and H_2S detection capacity (Scheme 1).

Increased H_2S selectivity from cooperative redox and combination reactions

Apart from its outstanding H_2S detection capacity and high stability, we also noticed that UC-PB_5 had ultra-high selectivity for H_2S among other biomolecules, including typical bioreductants and bio-complexes (Fig. S8 and 9†). Moreover, UC-PB_5 also showed no response to other bio-sulfur species (typically biothiols, $S_2O_3^{2-}$, and SO_3^{2-}), even at high concentrations (15 mM, 100-fold higher than [H_2S]; Fig. 2A and B). To uncover the mechanism of this ultra-highly selective H_2S detection, the reaction was monitored and products were characterized. After adding UC-PB_5 into a H_2S solution, the free S^{2-} concentration significantly decreased as a function of time, indicating that H_2S may have reacted with UC-PB_5 (Fig. 2C). However, because ferrocyanide (also known as Prussian White, reduced PB) can be rapidly oxidized by dissolved oxygen in water, the single redox reaction between UC-PB_5 and H_2S failed to achieve permanent PB decomposition according to dynamic absorbance spectra (Fig. 2D). Therefore, we concluded that the decomposition of PB by H_2S involved cooperation of both redox and combination reactions. To confirm this hypothesis, the products were further characterized. TEM images showed that small nanostructures were formed after adding H_2S, while PB shells were rugged and detached from UCNP surfaces (Fig. 2E). Square-wave voltammetry (SWV) curves and Fe_{2p} X-ray photoelectron spectroscopy (XPS) spectra suggested that the Fe(III) in PB was the oxidation reaction center (Fig. 2F and G), while the S_{2p} XPS spectra confirmed the existence of both sulfur and ferrous sulfide, demonstrating the simultaneous redox and combination reactions between UC-PB_5 and H_2S (Fig. 2H). As there were two coordinated Fe(II) in the reduced form of PB (Fe(II)–C≡N– and Fe(II)–N≡C–), the combination reaction center was further identified by studying the reaction between H_2S and other iron complexes. This showed that only sulfur was produced in the

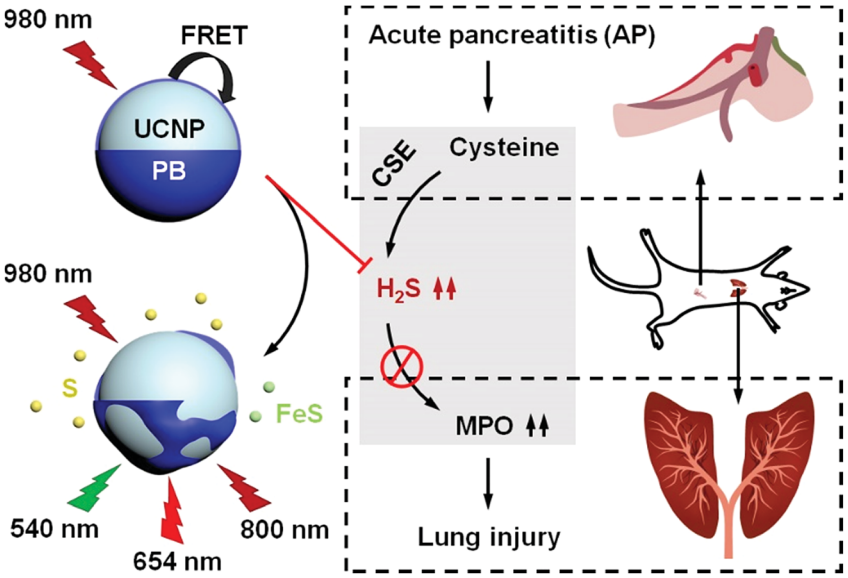

Scheme 1 Schematic illustrations of ultra-highly selective colorimetric/luminescence dual-modal H_2S detection and acute pancreatitis (AP)-associated lung injury alleviation using UC-PB_5 nanoprobes. CSE: cystathionine-γ-lyase; MPO: myeloperoxidase.

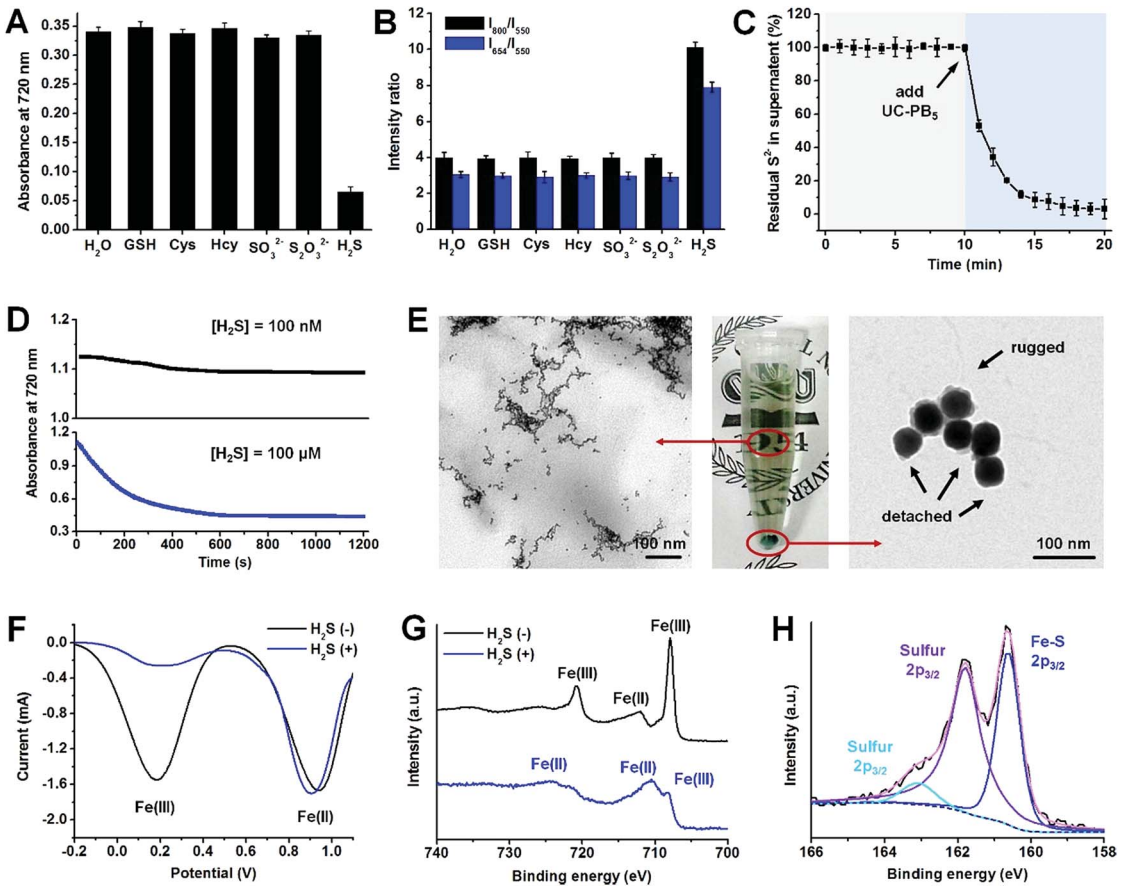

Fig. 2 Mechanism of ultra-high H_2S selectivity. Absorbance at 720 nm (A) and UCL ratio (B) of UC-PB_5 nanoprobes in response to various biogenic sulfur species. (C) Dynamic free S^{2-} amount in aqueous solution before and after addition of UC-PB_5 nanoprobes. (D) Dynamic absorbance of UC-PB_5 nanoprobes at 720 nm in response to relatively low (100 nM) and high (100 μM) concentrations of H_2S. (E) Photograph of the UC-PB_5 nanoprobe suspension after H_2S addition and centrifugation. TEM images of the supernatant (left) and precipitate (right). SWV curve (F) and Fe_{2p} XPS spectra (G) of UC-PB_5 nanoprobes with/without H_2S addition. (H) S_{2p} XPS spectra of UC-PB_5 nanoprobes with H_2S addition. Data are represented as mean ± SD.

reaction between ferricyanide (containing Fe(II)–C≡N– in its reduced form) and H_2S, while both sulfur and ferrous sulfide were produced between ferric isothiocyanate (containing Fe(II)–N≡C– in its reduced form) and H_2S, which was attributed to the stronger coordinative interaction between Fe(II) and C than N in the –C≡N– structure (Fig. S11†). Above all, the ultra-highly selective H_2S detection using UC-PB_5 contributed to the permanent PB decomposition by the cooperation of redox and combination reactions between H_2S and PB. The nitrogen-coordinated Fe was either the oxidation or combination reaction center in PB that reacted with H_2S, resulting in the H_2S-responsiveness of PB.

Ultra-highly selective ratiometric imaging of H_2S

By virtue of the fact that luminescence signals are essential resources for bioimaging, UC-PB_5 was a potential H_2S-responsive nanophosphor for imaging H_2S in cells and *in vivo*. The signal intensity obtained from luminescence imaging was also useful for evaluating the concentration of H_2S in regions or samples of interest. Before applying UC-PB_5 to further experimentation, its cytotoxicity and biocompatibility were carefully studied though the PB and upconversion nanoparticles were previously reported to be safe for bioapplications.[29,30] Both cell viability assays and SYTO-9/propidium iodide staining suggested that UC-PB_5 had no obvious cytotoxicity. It had relatively high IC_{50} values of 4.05 mg kg^{-1} and 3.44 mg kg^{-1} at 24 and 48 h, respectively (Fig. S12†). Furthermore, serological tests and tissue sections also suggested that UC-PB_5 had no negative influence on organ function or morphology, demonstrating its good *in vivo* biocompatibility (Fig. S13 and 14†). These results ensured the safety of UC-PB_5 in the subsequent studies.

It is known that H_2S can be produced from thiol-containing amino acids under the enzymatic catalysis of cystathionine-γ-lyase (CSE).[31] However, DL-propargylglycine (DL-PAG) can irreversibly inhibit CSE by attacking the active-site Tyr^{114} with its deprotonated β-position, resulting in reduced H_2S production.[32] In contrast, L-cysteine (L-Cys) and NaHS, which can serve as the substrate and product of this reaction, respectively, can correspondingly alter intracellular H_2S levels (Fig. S15A†). Thus, these biomolecules can modulate intracellular H_2S concentrations by simulating the environment and regulatory processes. Due to the correlation between the UCL ratio of nanoprobes and H_2S concentration, UC-PB_5 was feasible for evaluating changes in intracellular H_2S levels.

After incubation with UC-PB_5, strong UCL was observed in the cytoplasm of living cells, which demonstrated that UC-PB_5 could be taken up by cells, which then accumulated H_2S-generated electrolytes (Fig. 3A). Dynamic imaging of intracellular H_2S also demonstrated that UC-PB_5 could rapidly and sensitively respond to changes in the H_2S concentration (Fig. 3B). By obtaining UCL intensities from the green (550 ± 20 nm, Abbr. G) and red (650 ± 15 nm, Abbr. R) channels of cells without pretreatment, a standard R/G ratio was calculated and set as the normal intracellular H_2S concentration (R/G = 6.28 ± 0.36, Fig. S15B and C†), which corresponded to previous findings. Compared with cells without pretreatment, the R/G ratio (5.49 ± 0.13) in DL-PAG-pretreated cells was significantly lower. In contrast, L-Cys and NaHS pretreated cells had higher R/G ratios (6.92 ± 0.35 for L-Cys and 7.38 ± 0.59 for NaHS) than non-pretreated cells (Fig. S15B†). Importantly, we also found that co-pretreated cells also had a lower H_2S concentration (R/G = 5.97 ± 0.28, $^{**}p < 0.01$) than non-pretreated cells. These results confirmed that UC-PB_5 was applicable for the ratiometric imaging of intracellular H_2S and could evaluate intracellular H_2S concentrations *via* UCL ratios.

As excessive serum H_2S levels can be a potential factor for diagnosing AP, an AP mouse model was established and ratiometric UCL imaging was conducted to evaluate serum H_2S concentrations *in vivo* to verify the feasibility of the developed nanoprobes (Fig. 4A and B and S16†).[33] A strong UCL signal was observed in mice that received intravenous injections of UC-PB_5 (Fig. 4C). The UCL images of dissected organs suggested that UC-PB_5 primarily accumulated in the reticuloendothelial system of mice (Fig. S17†), which corresponded to the biodistribution and metabolic pathway of UC-PB_5 (Fig. S18†). It was clear that the UCL signals collected in both the NIR (800 ± 12 nm, Abbr. N) and green (550 ± 20 nm, Abbr. G) ranges from AP mice were higher than those from normal mice. The N/G ratio of AP mice was also significantly higher than that of normal mice (N/G = 9.28 ± 0.69 *vs.* 7.26 ± 0.75, $^{***}p < 0.001$; Fig. 4D). The strong UCL signal and high N/G ratio found in AP mice were attributed to the UCL recovery caused by the reaction between UC-PB_5 and high serum H_2S levels, which suggested that UC-PB_5 was a potential tool for diagnosing AP. More importantly, the CSE-inhibition effect of DL-PAG was also observed by UCL imaging *in vivo*. At 12 h post-injection of DL-PAG, the N/G ratio was decreased (N/G = 7.89 ± 0.86, $^{***}p < 0.001$) and significantly different compared with that of AP mice that received PBS. These results were in accordance with the studies of cultured cells and indicated that CES activity in AP mice could be effectively inhibited by DL-PAG. These results demonstrated the feasibility of using UC-PB_5 nanoprobes to evaluate H_2S concentration in cells and *in vivo* by ratiometric imaging, as well as their potential for diagnosing AP.

Alleviating AP-associated lung injury *in vivo* by H_2S elimination

Excessive serum H_2S levels in AP lead to various complications that can be even worse than AP itself.[34] Among these complications, H_2S-induced lung injury, including pneumonitis and acute respiratory distress syndrome, are the most serious and are directly responsible for the high early mortality rates in AP cases.[35] Therefore, simultaneously inhibiting H_2S production and eliminating H_2S serum could improve early survival rates.[36] However, traditional H_2S synthetase inhibitors like DL-PAG are slow-acting and cannot eliminate H_2S from serum.[37] To meet the requirements of clinical practice and overcome the limitations of H_2S synthetase inhibitors, it is essential to develop drugs with rapid H_2S elimination capacity. According to the results obtained from H_2S detection *in vitro* and H_2S imaging *in vivo*, the as-designed UC-PB_5 nanoprobes could rapidly react with H_2S, and thus are expected to eliminate serum H_2S within a short period with high efficiency, which would be

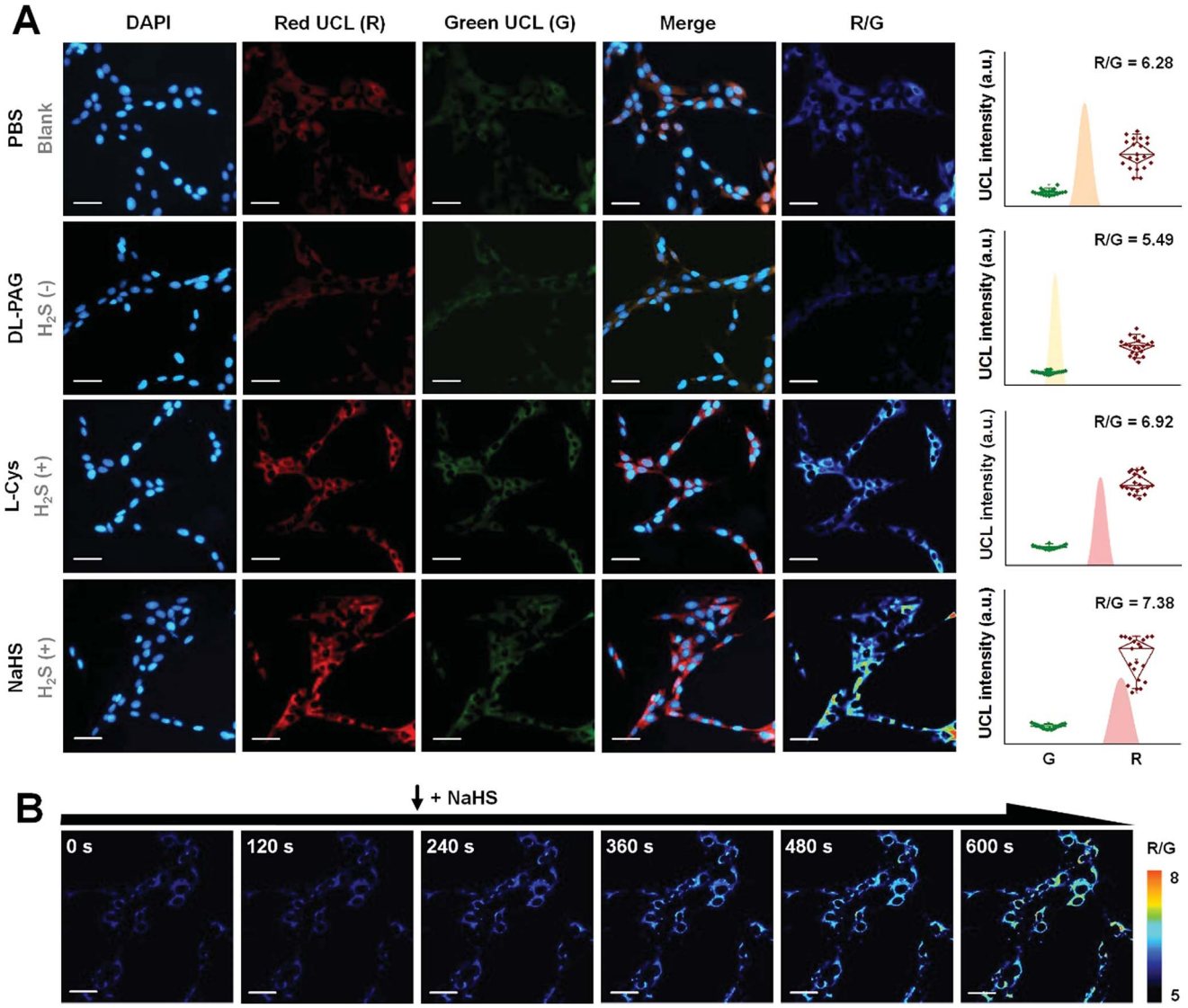

Fig. 3 Evaluation of the intracellular H_2S level by ultra-highly selective ratiometric imaging. (A) Luminescence images of A549 cells after various pre-treatments and incubation with UC-PB_5 nanoprobes. The nucleus was stained with commercial DAPI staining solution. The ratiometric luminescence images and R/G ratios were calculated from signals collected from the red channel (R) and green channel (G). The corresponding statistics of UCL signal intensity and calculated R/G ratios are also presented. (B) Dynamic ratiometric luminescence images of A549 cells incubated with UC-PB_5 nanoprobes before and after NaHS addition. The scale bar was 20 μm.

complementary to inhibitor-based drugs (Fig. S19A†). To test the H_2S-elimination effect of UC-PB_5, serum H_2S concentrations were determined in AP mice that received UC-PB_5 nanoprobe injections. These data showed that serum H_2S levels in AP mice that received DL-PAG decreased continuously over the first 3 h and remained lower than those in untreated AP mice for the next 2 h. Furthermore, serum H_2S levels in AP mice that received UC-PB_5 were significantly reduced over the first 2 h of post-injection, which suggested that UC-PB_5 rapidly affected serum H_2S levels after intravenous injection (Fig. 4E). To test for synergistic effects of UC-PB_5 and DL-PAG on H_2S levels, AP mice were co-injected with the two agents. Interestingly, serum H_2S levels were close to the levels in control mice over the study period, which demonstrated that UC-PB_5 and DL-PAG synergistically eliminated H_2S from serum.

In most cases, H_2S-induced lung injury is associated with abnormal myeloperoxidase (MPO) activation in the lungs, which results in the overproduction of hypochlorous acids and oxidative damage.[38] Thus, pulmonary MPO activity was also determined to further illustrate the synergy between UC-PB_5 and DL-PAG in alleviating lung injury (Fig. 4F). These data demonstrated that MPO activity was significantly decreased in the lungs of AP mice that received both treatments compared with those that received no or single treatment (UC-PB_5 nanoprobes or DL-PAG), and was correlated with the decreased serum H_2S levels; hematoxylin and eosin-stained sections also supported these findings (Fig. 4G and H). Lungs harvested from mice that received both treatments had reduced inflammatory reactions and milder pulmonary interstitial edema at the same time points compared with the other mice (Fig. S19B†). These

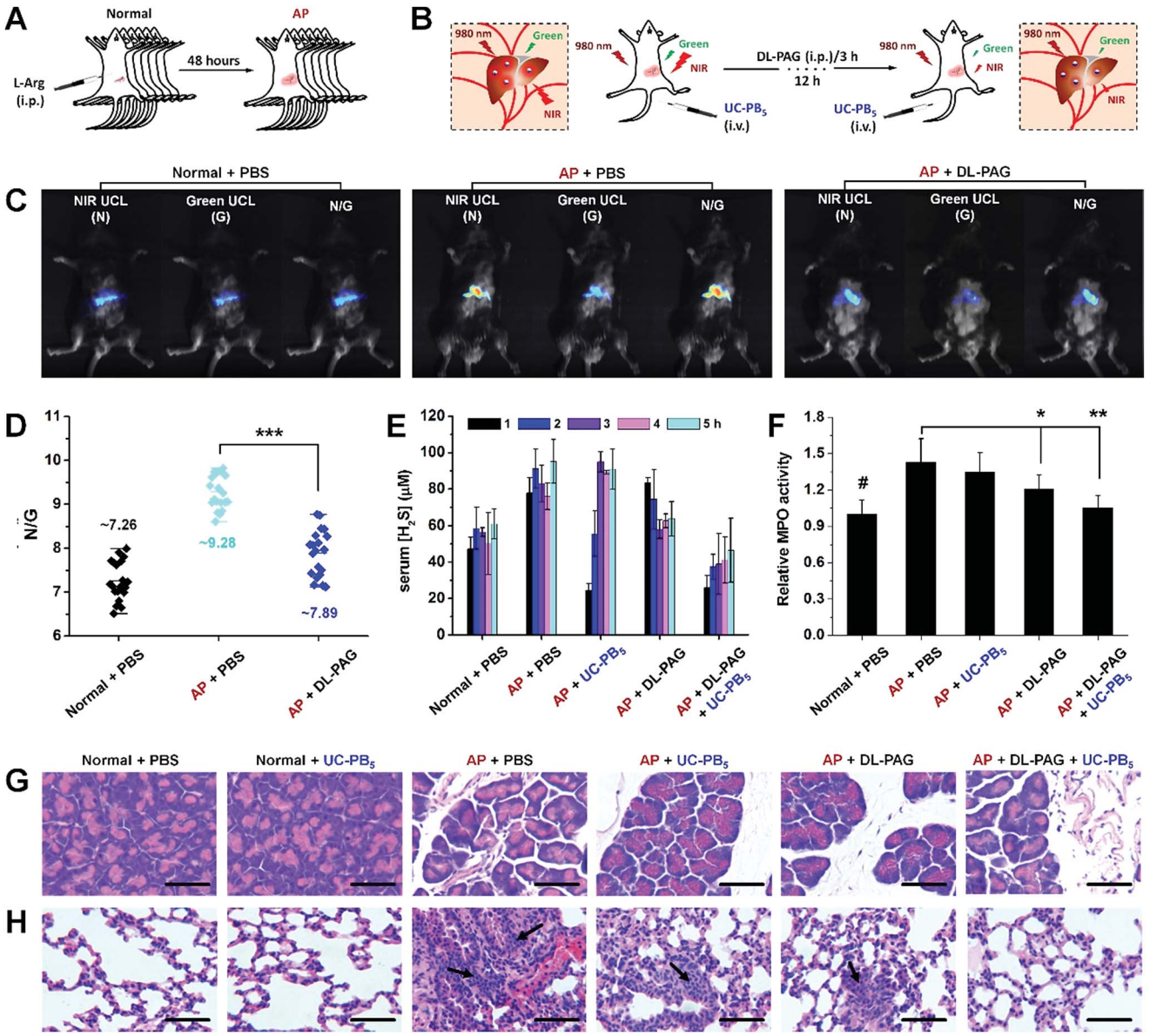

Fig. 4 Evaluation of the serum H_2S level and alleviation of AP-associated lung injury *in vivo*. Schematic illustrations of AP model establishment (A) and theranostics experiments (B). Luminescence images (C) and UCL ratio (D) obtained from mice after various pre-treatments and intravenous injection of UC-PB_5 nanoprobes. (E) H_2S concentration in serum of mice that received various treatments in the course of 5 h. (F) Relative MPO activity in the lungs of mice that received various treatments. H&E-stained sections of pancreases (G) and lungs (H) harvested from mice that received various treatments. Statistical significance was determined from one-way *t* tests. *$p < 0.05$, **$p < 0.01$, and ***$p < 0.001$. The scale bar was 50 μm. L-Arg: L-arginine; #: the group as the standard of normalization. Data are represented as mean ± SD.

results suggested that co-treatment with UC-PB_5 and DL-PAG synergistically alleviated AP-associated lung injury by eliminating H_2S from serum and inhibiting H_2S production, respectively.

Conclusion

In summary, rationally designed pure-inorganic upconversion nanoprobes using PB as a H_2S-responsive acceptor were developed for sensitive and ultra-highly selective H_2S detection, imaging, and elimination. To meet the serum H_2S concentration range, upconversion nanoprobes with 5 nm PB shells (UC-PB_5) were optimized for *in vivo* studies. The UC-PB_5 nanoprobes not only possessed outstanding H_2S detection capacity *in vitro* (linear range: 0–150 μM, LOD: 50 nM), but were also feasible for H_2S imaging in cells and in an AP mouse model. Moreover, the rapid H_2S elimination by UC-PB_5, in cooperation with the long-term inhibition of H_2S production by DL-PAG, effectively inhibited H_2S-associated MPO activation, which further reduced the oxidative stress in the lungs, alleviating AP-associated lung injury. As PB is an approved drug, our work highlights its great potential for clinical AP treatment by alleviating lung injury, which could reduce the early mortality rate of AP.

Author contributions

Y. L. and J. Z. conceived the project, analyzed the results, and wrote the original manuscript. All authors contributed to the preparation of the original and revised manuscripts. Y. L., Q. J., and X. Z. synthesized the UC-PB nanoprobes. Y. L., A. J., and F. M. investigated the characteristics of the UC-PB nanoprobes. Y. L. and X. Z. performed UCL imaging *in vitro* and *in vivo*. Y. L. and Q. J. conducted the other experiments.

Conflicts of interest

There are no conflicts to declare.

Acknowledgements

The authors are thankful for the funding from the Beijing Talent Foundation Outstanding Young Individual Project (2015000026833ZK02), The Joint Foundation Program of Beijing Municipal Natural Science Foundation and Beijing Municipal Education Commission (KZ201810028045), Capacity Building for Sci-Tech Innovation-Fundamental Scientific Research Funds (025185305000/195), Project of High-level Teachers in Beijing Municipal Universities in the Period of the 13th Five-year Plan (IDHT20180517), Project of Construction of Scientific Research Base by the Beijing Municipal Education Commission, Yanjing Young Scholar Development Program of Capital Normal University, and Youth Innovative Research Team of Capital Normal University.

References

1 P. Rose, P. K. Moore and Y.-Z. Zhu, *Trends Pharmacol. Sci.*, 2018, **39**, 624–634.
2 M. Bhatia, F. L. Wong, D. Fu, H. Y. Lau, S. M. Moochhala and P. K. Moore, *FASEB J.*, 2005, **19**, 623–625.
3 P. G. Lankisch, M. Apte and P. A. Banks, *Lancet*, 2015, **386**, 85–96.
4 S. Chen, A. Z. Weitemier, X. Zeng, L. He, X. Wang, Y. Tao, A. J. Y. Huang, Y. Hashimotodani, M. Kano, H. Iwasaki, L. K. Parajuli, S. Okabe, D. B. L. Teh, A. H. All, I. Tsutsui-Kimura, K. F. Tanaka, X. Liu and T. J. McHugh, *Science*, 2018, **359**, 679–684.
5 M.-H. Chan, Y.-T. Pan, Y.-C. Chan, M. Hsiao, C.-H. Chen, L. Sun and R.-S. Liu, *Chem. Sci.*, 2018, **9**, 3141–3151.
6 C. Li, Y. Zhang, G. Chen, F. Hu, K. Zhao and Q. Wang, *Adv. Mater.*, 2017, **29**, 1605754.
7 X. Li, X. Tong, Y. Yin, H. Yan, C. Lu, W. Huang and Q. Zhao, *Chem. Sci.*, 2017, **8**, 5930–5940.
8 P. Zhang, H. Wang, Y. Hong, M. Yu, R. Zeng, Y. Long and J. Chen, *Biosens. Bioelectron.*, 2018, **99**, 318–324.
9 P. Zhang, X.-f. Jiang, X. Nie, Y. Huang, F. Zeng, X. Xia and S. Wu, *Biomaterials*, 2016, **80**, 46–56.
10 P. Zhang, X. Nie, M. Gao, F. Zeng, A. Qin, S. Wu and B. Z. Tang, *Mater. Chem. Front.*, 2017, **1**, 838–845.
11 P. Zhang, Y. Tian, H. Liu, J. Ren, H. Wang, R. Zeng, Y. Long and J. Chen, *Chem. Commun.*, 2018, **54**, 7231–7234.
12 X. Zhu, Q. Su, W. Feng and F. Li, *Chem. Soc. Rev.*, 2017, **46**, 1025–1039.
13 L. Sun, R. Wei, J. Feng and H. Zhang, *Coord. Chem. Rev.*, 2018, **364**, 10–32.
14 W. Wei, G. Chen, A. Baev, G. S. He, W. Shao, J. Damasco and P. N. Prasad, *J. Am. Chem. Soc.*, 2016, **138**, 15130–15133.
15 W. Fan, W. Bu and J. Shi, *Adv. Mater.*, 2016, **28**, 3987–4011.
16 J. Xu, W. Han, Z. Cheng, P. Yang, H. Bi, D. Yang, N. Niu, F. He, S. Gai and J. Lin, *Chem. Sci.*, 2018, **9**, 3233–3247.
17 L. Zhou, Y. Fan, R. Wang, X. Li, L. Fan and F. Zhang, *Angew. Chem., Int. Ed.*, 2018, **57**, 12824–12829.
18 Y. Liu, A. Jiang, Q. Jia, X. Zhai, L. Liu, L. Ma and J. Zhou, *Chem. Sci.*, 2018, **9**, 5242–5251.
19 X. Hu, Y. Wang, H. Liu, J. Wang, Y. Tan, F. Wang, Q. Yuan and W. Tan, *Chem. Sci.*, 2017, **8**, 466–472.
20 P. Huang, W. Zheng, S. Zhou, D. Tu, Z. Chen, H. Zhu, R. Li, E. Ma, M. Huang and X. Chen, *Angew. Chem., Int. Ed.*, 2014, **53**, 1252–1257.
21 Q. Su, W. Feng, D. Yang and F. Li, *Acc. Chem. Res.*, 2017, **50**, 32–40.
22 B. Gu and Q. Zhang, *Adv. Sci.*, 2018, **5**, 1700609.
23 J. Peng, C. L. Teoh, X. Zeng, A. Samanta, L. Wang, W. Xu, D. Su, L. Yuan, X. Liu and Y.-T. Chang, *Adv. Funct. Mater.*, 2015, **26**, 191–199.
24 Y. Zhou, W. Chen, J. Zhu, W. Pei, C. Wang, L. Huang, C. Yao, Q. Yan, W. Huang, J. S. C. Loo and Q. Zhang, *Small*, 2014, **10**, 4874–4885.
25 B. Kong, C. Selomulya, G. Zheng and D. Zhao, *Chem. Soc. Rev.*, 2015, **44**, 7997–8018.
26 Y. Liu, Q. Guo, X. Zhu, W. Feng, L. Wang, L. Ma, G. Zhang, J. Zhou and F. Li, *Adv. Funct. Mater.*, 2016, **26**, 5120–5130.
27 S. Liu, L. Zhang, T. Yang, H. Yang, K. Y. Zhang, X. Zhao, W. Lv, Q. Yu, X. Zhang, Q. Zhao, X. Liu and W. Huang, *ACS Appl. Mater. Interfaces*, 2014, **6**, 11013–11017.
28 Z. Gao, L. Wang, L. Wang and H. Chen, *Anal. Methods*, 2017, **9**, 835–840.
29 L. Cheng, H. Gong, W. Zhu, J. Liu, X. Wang, G. Liu and Z. Liu, *Biomaterials*, 2014, **35**, 9844–9852.
30 A. Gnach, T. Lipinski, A. Bednarkiewicz, J. Rybka and J. A. Capobianco, *Chem. Soc. Rev.*, 2015, **44**, 1561–1584.
31 G. Yang, L. Wu, B. Jiang, W. Yang, J. Qi, K. Cao, Q. Meng, A. K. Mustafa, W. Mu, S. Zhang, S. H. Snyder and R. Wang, *Science*, 2008, **322**, 587–590.
32 D. Ezeriņa, Y. Takano, K. Hanaoka, Y. Urano and T. P. Dick, *Cell Chem. Biol.*, 2018, **25**, 447–459.
33 M. Bhatia, in *Methods Enzymol.*, ed. E. Cadenas and L. Packer, 2015, vol. 555, pp. 195–205.
34 M. Bhatia, A. K. Saluja, B. Hofbauer, J.-L. Frossard, H. S. Lee, I. Castagliuolo, C.-C. Wang, N. Gerard, C. Pothoulakis and M. L. Steer, *Proc. Natl. Acad. Sci. U. S. A.*, 1998, **95**, 4760–4765.
35 T. Dombernowsky, M. Ø. Kristensen, S. Rysgaard, L. L. Gluud and S. Novovic, *Pancreatology*, 2016, **16**, 756–760.
36 R. K. Velusamy and R. Tamizhselvi, *J. Pharm. Pharmacol.*, 2018, **70**, 1188–1199.
37 Z. Qu, Y. Jiang, B.-Q. Wu, Y.-F. Duan, Z.-D. Sun and G.-H. Luo, *Arch. Med. Sci.*, 2014, **10**, 825–829.
38 A. Warris and E. R. Ballou, *Semin. Cell Dev. Biol.*, 2018, DOI: 10.1016/j.semcdb.2018.1003.1004.

